The Astrophysical Journal Letters, 961:L22 (14pp), 2024 January 20 https://doi.org/10.3847/2041-8213/ad18c7

Explosive Nucleosynthesis in Core-collapse Type II Supernovae: Insights from New C, N, Si, and Al–Mg Isotopic Compositions of Presolar Grains

Nan Liu[1,2], Conel M. O'D. Alexander[3], Bradley S. Meyer[4], Larry R. Nittler[3,5], Jianhua Wang[3], and Rhonda M. Stroud[5]
[1] Institute for Astrophysical Research, Boston University, Boston, MA 02215, USA; nanliu@bu.edu
[2] Physics Department and McDonnell Center for the Space Sciences, Washington University in St. Louis, St. Louis, MO 63130, USA
[3] Earth and Planets Laboratory, Carnegie Institution for Science, Washington, DC 20015, USA
[4] Department of Physics and Astronomy, Clemson University, Clemson, SC 29634, USA
[5] School of Earth and Space Exploration, Arizona State University, Tempe, AZ 85281, USA
Received 2023 September 10; revised 2023 November 29; accepted 2023 December 8; published 2024 January 17

Abstract

We report C, N, Si, and Al–Mg isotope data for 39 presolar X silicon carbide (SiC) and four silicon nitride grains —a group of presolar grains that condensed in the remnants of core-collapse Type II supernovae (CCSNe)— isolated from the Murchison meteorite. Energy dispersive X-ray data were used to determine the Mg and Al contents of the X SiC grains for comparison with the Mg/Al ratios determined by secondary ion mass spectroscopy (SIMS). Previous SIMS studies have used O-rich standards in the absence of alternatives. In this study, the correlated isotopic and elemental data of the X SiC grains enabled accurate determination of the initial $^{26}Al/^{27}Al$ ratios for the grains. Our new grain data suggest that (i) the literature data for X grains are affected to varying degrees by asteroidal/terrestrial contamination, and (ii) the Al/Mg ratios in SiC are a factor of 2 (with $\pm 6\%$ 1σ uncertainties) lower than estimated based on the SIMS analyses that used O-rich standards. The lowered Al/Mg ratios result in proportionally higher inferred initial $^{26}Al/^{27}Al$ ratios for presolar SiC grains. In addition, the suppression of asteroidal/terrestrial contamination in this study leads to the observation of negative trends for $^{12}C/^{13}C$–$^{30}Si/^{28}Si$ and $^{26}Al/^{27}Al$–$^{30}Si/^{28}Si$ among our CCSN grains. We discuss these isotope trends in the light of explosive CCSN nucleosynthesis models, based on which we provide new insights into several nontraditional CCSN nucleosynthesis processes, including explosive H burning, the existence of a C/Si zone in the outer regions of CCSNe, and neutrino–nucleus reactions in deep CCSN regions.

Unified Astronomy Thesaurus concepts: Circumstellar matter (241); Stellar astronomy (1583); Circumstellar dust (236); Nucleosynthesis (1131); Type II supernovae (1731)

1. Introduction

Core collapse Type II supernovae (CCSNe) are important in cosmic evolution because they are responsible for the creation and dissemination of many of the heavy elements that are necessary for the formation of planets and life, including C, N, and O (Kobayashi et al. 2020). CCSNe also may have played a critical role in the formation and early evolution of the solar system by providing short-lived radionuclides (e.g., Takigawa et al. 2008) and/or isotopically anomalous material responsible for large-scale isotopic variations across the protoplanetary disk (e.g., Nie et al. 2023). Quantifying the contributions of CCSNe to these cosmic events demands accurate CCSN nucleosynthesis model predictions, which, however, are hampered by uncertainties in neutrino transport, the progenitor star properties, the hydrodynamics of the explosion, and nuclear reaction rates (Limongi & Chieffi 2003). Direct observations of isotope abundances in CCSNe are ideal for testing and constraining CCSN nucleosynthesis models, but such measurements, so far, are available for only a few radioactive isotopes such as ^{56}Ni ($t_{1/2} = 6$ days) and ^{44}Ti ($t_{1/2} = 60$ a) (e.g., Diehl 2017).

Presolar grains from CCSNe that exploded before solar system formation, such as Type X silicon carbide (SiC) grains and silicon nitride (Si_3N_4) grains (hereafter both are referred to as CCSN grains), provide us with a unique opportunity to directly constrain CCSN nucleosynthesis models. The CCSN origin of X and Si_3N_4 grains is supported by the inferred initial presence of ^{44}Ti along with many other diagnostic isotopic signatures, including high abundances of ^{26}Al ($t_{1/2} = 7.2 \times 10^5$ a) inferred from excess amounts of the decay product ^{26}Mg (Nittler & Ciesla 2016). Micron-sized CCSN grains have been measured in the laboratory using modern mass spectrometers for isotope ratios of many elements from C to Ba with percent-level precisions (Liu et al. 2022), thus enabling testing of CCSN models in unprecedented detail. However, several factors have constrained or compromised previous isotopic studies of CCSN grains to varying degrees, as summarized below. (i) Among presolar SiC grains, X grains are quite low in abundance (1%–2%), and it is thus time-, cost-, and labor-intensive to locate a sufficient number of samples to provide statistically meaningful data. Presolar Si_3N_4 grains are even rarer, being about 1 order of magnitude lower in abundance than presolar X SiC grains (Nittler et al. 1995). (ii) Presolar CCSN grains are submicron to micron in size, making their analysis challenging. For instance, Groopman et al. (2015) demonstrated that the literature X SiC grain data suffered from terrestrial and/or asteroidal Al contamination, resulting in deviations of the derived initial $^{26}Al/^{27}Al$ data from the true compositions to varying degrees. (iii) Presolar CCSN grain data represent the compositions of CCSN ejecta at a small scale (e.g., millimeters or larger, depending on the gas density/pressure), and the accuracy of predicted ejecta compositions at

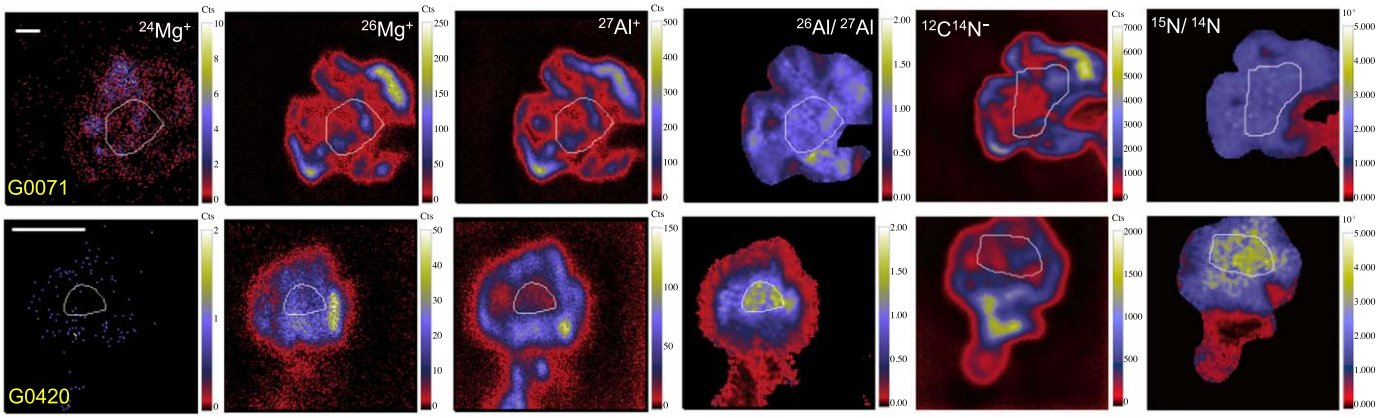

Figure 1. NanoSIMS ion and isotope images of two X SiC grains from this study that had relatively low (M5-A5-G0071) and high (M5-A3-G0420) levels of Al contamination. The scale bar and contour line denotes 500 nm and the region of interest (ROI) for data reduction, respectively. The ROIs were chosen to maximally suppress N or Al contamination and/or topographic effects. The isotope ratio images were calculated using the same method as adopted for the isotope data reported in Table 1.

such fine spatial resolution remains unknown, especially given the complexity in the hydrodynamics of the explosions (Müller 2020).

In this study, we maximized the efficiency of locating CCSN grains by adopting our previously developed backscattered electron-energy dispersive X-ray (BSE-EDX) screening method (Liu et al. 2017), which led to the identification of 51 X SiC and four Si_3N_4 grains in total. We optimized the spatial resolution in Al–Mg isotope analyses by using a nanoscale secondary ion mass spectrometer (NanoSIMS) equipped with a Hyperion radio-frequency plasma O^- ion source (Malherbe et al. 2016). The ∼100 nm spatial resolution in all NanoSIMS ion images (Figure 1) enabled recognition and exclusion of extrinsic contamination that had not been fully removed by presputtering.[6] Here, we report C, N, Si, and inferred initial $^{26}Al/^{27}Al$ isotope ratios for 43 of the CCSN grains that were ≥500 nm. We discuss how CCSN stellar nucleosynthesis and mixing could yield the isotope trends that we observe in the data, instead of reproducing the composition of each grain by ad hoc mixing calculations as done previously. Our data-model comparison approach minimizes the effect of the bottleneck (iii) and can yield more accurate constraints on CCSN models.

2. Analytical Methods and CCSN Model Simulations

The SiC grains in this study were extracted from the Murchison (CM2) carbonaceous chondrite by means of the CsF dissolution technique described in Nittler & Alexander (2003). SiC and Si_3N_4 grains on mounts #5 and #6 were first identified by automatic BSE-EDX particle analyses by following the procedure described in Liu et al. (2017). The BSE-EDX analyses were conducted with the Carnegie JEOL 6500F field emission scanning electron microscope (SEM) equipped with an Oxford Instruments silicon drift detector. The EDX data were obtained as 30 s point measurements with a 10 kV, 1 nA electron beam at the center of each particle. We focused on Mg-rich (>0.1 wt%) SiC grains since their high Mg contents are indicative of their high initial $^{26}Al/^{27}Al$ ratios and thus their CCSN origins (Liu et al. 2017). Si_3N_4 grains were identified by their EDX spectra. Given the similarities in the isotopic compositions of X SiC and Si_3N_4 grains (Nittler et al. 1995; Lin et al. 2010), we will discuss all CCSN grain data together without distinguishing between the two phases.

We measured grains on mount #5 and mount #6 with the Washington University NanoSIMS 50 and Carnegie NanoSIMS 50L ion microprobes, respectively, for C, Si, and N isotopes, based on which 51 X SiC and four Si_3N_4 grains were identified. In all the NanoSIMS sessions, a Cs^+ beam of ∼9 and ∼1 pA was used for presputtering and analysis, respectively. Prior to an actual analysis, we presputtered each grain until all ion count rates became constant, which generally took 1–3 minutes. During presputtering, the $^{12}C^{14}N^-$ count rate often decreased over time, suggesting the presence of surface N contamination. Any remaining contaminant that could be recognized in NanoSIMS ion images were further excluded by choosing small regions of interest (ROIs) during data reduction (Figure 1). Among the 55 identified CCSN grains, 43 large (≥500 nm) SiC and Si_3N_4 grains were further analyzed for their Al–Mg isotopes with the Carnegie NanoSIMS 50L ion microprobe following the procedures reported in Liu et al. (2018a). For Al–Mg isotopes, an O^- beam of ∼3 pA and ∼1 pA was used for presputtering and analysis, respectively. Despite the often-observed Al-rich contamination rims around presolar SiC grains (e.g., G0420 in Figure 1), we did not observe decreasing Al^+ count rate during presputtering, likely because the previous extensive NanoSIMS analyses had already exposed clean surfaces by removing surface Al contamination. Polished NIST 610 glass and fine-grained (1–3 μm) Burma spinel ($MgAl_2O_4$) grains were both measured as standards during the Al–Mg isotope analysis session. All the C, N, Si, and Al–Mg isotope data were collected using electron multipliers in imaging mode at a spatial resolution of ∼100 nm (Figure 1).

The initial $^{26}Al/^{27}Al$ ratio was calculated from the equation $^{26}Al/^{27}Al = [^{26}Mg_{grain} - {}^{24}Mg_{grain} \times \left(\frac{26Mg}{24Mg}\right)_{std}]/(^{27}Al_{grain} \times \Gamma_{Mg/Al})$, in which $\Gamma_{Mg/Al}$ denotes the SIMS Mg/Al relative sensitivity factor. The $\Gamma_{Mg/Al}$ value was determined to be 1.34 ± 0.18 (1σ) and 1.22 ± 0.08 based on NanoSIMS analyses of the NIST 610 and spinel standards, respectively. Based on NIST 610, we determined the $\Gamma_{Mg/Si}$ and $\Gamma_{Al/Si}$ values to be 5.31 ± 0.57 and 3.96 ± 0.31, respectively. The errors in the

[6] Presputtering refers to the process of removing a layer of material from the surface of a sample before the actual analysis begins, allowing for exposing a clean surface and reaching a state of chemical equilibrium to maintain stable count rates during the subsequent secondary ion mass spectrometric (SIMS) analysis.

610-derived values are dominated by uncertainties in the elemental abundances reported in the literature[7] (Pearce et al. 1997). The C, N, Si, and initial $^{26}Al/^{27}Al$ isotope data are reported in Table 1 with 1σ errors. Here, we will focus on these isotope systems to illustrate the necessary role of supernova core material in shaping the isotopic compositions of CCSN grains.

The EDX data were quantified with Oxford Aztec routines using a suite of pure elemental and oxide standards (see Liu et al. 2017 for details). To investigate differential X-ray absorption effects on particle EDX measurements, we performed Monte Carlo simulations of the X-ray yields for SiC with wt% levels of Mg and Al with the CASINO 2.51 software (Figure A1 in Appendix A).

For comparison with the CCSN grain data from this study, we will adopt the set of CCSN nucleosynthesis calculations reported in Liu et al. (2018b). These calculations explored explosive nucleosynthesis based on the 25 $M_\odot$ presupernova star model of Rauscher et al. (2002) and the explosion model and reaction network of Bojazi & Meyer (2014). The calculations were run at explosion energies, E, ranging from 1×10^{51} to 5×10^{51} erg, and did not include neutrino–nucleus interactions. In this study, we repeated the nucleosynthesis calculations by implementing neutrino reactions (with neutrino–nucleus reaction rates from Meyer et al. 1998b) because we are interested in deep CCSN layers that are close to the collapsing stellar core, where the neutrino flux is high enough to affect the nucleosynthesis of interest. We also extended E to 10×10^{51} erg in both sets of calculations. We will refer to the two sets of calculations as ν- and no-ν-models. We will discuss the nucleosynthesis calculations by dividing the CCSN layers into different zones that are labeled by the two most abundant elements that they contain (Meyer et al. 1995).

3. Results and Discussion

3.1. Calibrating $\Gamma_{Mg/Al}$ in Presolar SiC

An accurate determination of the initial $^{26}Al/^{27}Al$ ratio is hampered by uncertainties in $\Gamma_{Mg/Al}$ that is commonly calibrated by measuring Burma spinel (e.g., Hoppe et al. 2023). Such an O-rich standard differs significantly from SiC and Si_3N_4 in the sample matrix, which raises the question whether the adopted calibration procedure is appropriate. Coordinated EDX and NanoSIMS analyses of X SiC grains provide us a unique opportunity to calibrate $\Gamma_{Mg/Al}$ in SiC more accurately for the following reasons. (i) Although presolar SiC grains are poor in Mg because of their high condensation temperatures (Lodders & Fegley 1995), X SiC grains are an exception because of the abundant radiogenic ^{26}Mg from ^{26}Al decay. Their high ^{26}Mg abundances enable direct determination of $^{26}Mg/^{27}Al$ (i.e., initial $^{26}Al/^{27}Al$) by EDX analysis that is, in principle, much less affected by matrix effects than NanoSIMS analysis. (ii) X grains serve as the best standard for calibrating $\Gamma_{Mg/Al}$ in presolar SiC grains since X grains closely resemble the other groups of SiC grains in trace element abundances, grain size, and grain morphology.

Our CASINO simulations (Figure A1) confirm that differential X-ray absorption effects were negligible for our measurements, thus justifying our method of deriving elemental abundances from the EDX spectra of small particles. We calculated the $(^{26}Mg/Si)_{EDX}$ ratios from the particle spectra by assuming that the Mg EDX peak consists of pure ^{26}Mg (Figure 2(a)). This assumption is supported by the NanoSIMS ion images, based on which we estimate that the contributions of ^{24}Mg and ^{25}Mg to the Mg budgets of the grains are negligible (i.e., mostly below 1%). In contrast, we observed significant amounts of Al contamination in the Mg–Al ion images of our CCSN grains. The effect of Al contamination on the SIMS data is illustrated in the lower panels of Figure 1 for grain M5-A3-0420: its rim has a higher Al concentration and lower $^{26}Al/^{27}Al$ ratio than its core, corroborating the effect of asteroidal/terrestrial Al contamination at the rim. Since our CASINO simulations show that EDX measurements with a 10 kV electron beam provide Al X-ray signals predominantly from depths of 200–600 nm below the sample surface (Figure A1), the contributions of Al X-rays from surface contamination to the total amounts sampled by EDX measurements are somewhat suppressed.

EDX and NanoSIMS analyses sample signals from a 1 μm^3 volume and a ~10 nm thin layer, respectively. A correlation is thus expected between EDX- and NanoSIMS-derived elemental ratios only if EDX and NanoSIMS analyses sampled materials from chemically homogenous grains. Therefore, we selected 19 well-isolated X SiC grains that exhibited relatively uniform $^{26}Mg^+$ distributions in their NanoSIMS ion images (denoted in Table 1). For instance, grain M5-A5-00071 was not selected because it exhibits locally enhanced $^{26}Mg^+$ by a factor of 10 within the chosen ROI (upper panels of Figure 1), pointing to a heterogenous distribution of $^{26}Mg^+$ that is likely caused by the presence of Al-rich subgrains; in comparison, despite the significant Al contamination at its rim, grain M3-G0420 was selected because it had a relatively constant $^{26}Mg^+$ content. Figure 2(a) shows that given $R = 0.96$, the Mg/Si ratios of the 19 X grains based on EDX and NanoSIMS analyses are well correlated. The same set of CCSN grains, however, is poorly correlated in the case of Al/Si ratio with $R = 0.54$ and MSWD = 30.9, likely resulting from the varying degrees of Al contamination (Figure 1) that were sampled by EDX analyses because of the poor spatial resolution (~1 μm). To suppress the effect of Al contamination, we analyzed a suite of large (>1 μm) mainstream (MS) presolar SiC grains, the dominant type of presolar SiC grains, on mount #5 for their Al–Mg isotopes using NanoSIMS (Figure A3). From the analyzed large MS grains, we selected 31 MS grains (Figure 2(b)) for deriving $\Gamma_{Al/Si}$ that had the least amounts of Al contamination (i.e., no obvious Al-rich rims) and relatively homogenous Al distributions (i.e., no significant local Al enrichments). The slopes of the linear fits in Figures 2(a) (0.740 ± 0.040) and 2(b) (0.379 ± 0.011) point to a true $\Gamma_{Mg/Al}$ value of 0.69 ± 0.04,[8] which is about a factor of 2 lower than estimated from Burma spinel (1.22 ± 0.08) and NIST 610 (1.34 $\pm$0.18). Since the R values of both linear correlations in Figure 2 are close to unity, we infer that their large MSWD values could have been caused by the following factors. (i) We likely underestimated the uncertainties in the derived elemental ratios because, for instance, we could not accurately account for uncertainties caused by topographic effects on the NanoSIMS analyses. (ii) Given the much larger MSWD value

[7] We adopted the overall average values from Table 1 of Pearce et al. (1997) for the composition of NIST 610. The calculated atomic Mg/Si, Al/Si, and Mg/Al ratios of NIST 610 glass standard are $(1.40 \pm 0.15) \times 10^{-3}$, $(3.43 \pm 0.27) \times 10^{-2}$, and $(4.08 \pm 0.53) \times 10^{-2}$, respectively.

[8] $\Gamma^{SiC}_{Mg/Al} = \Gamma^{NIST610}_{Mg/Al}/(0.740/0.379) = 1.34/1.95 = 0.69$.

Table 1
Isotope and Elemental Ratio Data of 39 X SiC and Four Si_3N_4 Grains from This Study (1σ Errors)

Grain	Phase	Subtype	Size (μm)	$^{12}C/^{13}C$	$^{14}N/^{15}N$	$\delta^{29}Si_{28}$ (‰)[a]	$\delta^{30}Si_{28}$ (‰)	$^{26}Al/^{27}Al$[b]	NanoSIMS[c]		EDX	
									$^{26}Mg/Si$ ($\times 10^{-3}$)	$^{27}Al/Si$($\times 10^{-3}$)	$^{26}Mg/Si$ ($\times 10^{-3}$)	$^{27}Al/Si$ ($\times 10^{-3}$)
M5-A1-0522[d]	SiC	X1	2.2	103.9 ± 0.9	58.6 ± 1.3	−199 ± 5	−360 ± 6	0.57 ± 0.01	6.0 ± 0.6	18.7 ± 1.4	3.0 ± 0.7	8.1 ± 0.9
M5-A2-0022[d]	SiC	X1	0.7	203.2 ± 8.6	76.4 ± 1.2	−250 ± 19	−387 ± 12	0.60 ± 0.04	8.4 ± 0.9	29.9 ± 3.9	6.6 ± 1.6	9.6 ± 1.6
M5-A2-1614	SiC	X2	0.6	15.8 ± 0.2	13.5 ± 0.2	−321 ± 14	−263 ± 14	0.84 ± 0.06	5.6 ± 0.6	14.2 ± 1.9	4.7 ± 1.8	7.2 ± 2.0
M5-A2-2885[d]	SiC	X2	1.5	608.6 ± 27.6	79.0 ± 1.3	−559 ± 11	−576 ± 6	1.01 ± 0.06	11.4 ± 1.2	24.1 ± 3.2	11.8 ± 1.0	16.4 ± 1.0
M5-A2-4297	SiC	X1	1.2	32.6 ± 0.4	49.9 ± 1.1	−145 ± 15	−230 ± 12	0.39 ± 0.03	7.2 ± 0.8	39.4 ± 5.2	3.9 ± 0.8	9.7 ± 1.0
M5-A2-4351[d]	SiC	X2	0.7	176.3 ± 6.0	47.2 ± 0.8	−499 ± 12	−624 ± 6	1.01 ± 0.06	26.6 ± 2.9	56.5 ± 7.4	19.1 ± 1.3	27.6 ± 1.4
M5-A3-0082	SiC	X1	1.0	154.2 ± 5.0	91.4 ± 3.0	−165 ± 20	−329 ± 9	0.70 ± 0.04	6.4 ± 0.7	19.8 ± 2.6	4.9 ± 0.8	7.2 ± 0.8
M5-A3-0132[d]	SiC	X1	1.0	643.8 ± 44.9	67.4 ± 1.3	−325 ± 18	−426 ± 11	0.83 ± 0.05	26.6 ± 2.9	68.5 ± 9.0	16.4 ± 1.1	23.5 ± 1.2
M5-A3-0420[d]	SiC	X1	1.3	25.2 ± 0.6	28.3 ± 0.5	−273 ± 16	−417 ± 6	1.14 ± 0.07	2.9 ± 0.3	5.4 ± 0.7	2.8 ± 0.8	6.4 ± 0.8
M5-A3-0946	SiC	X2	1.3	1059.1 ± 65.0	55.8 ± 0.9	−587 ± 9	−453 ± 11	1.07 ± 0.07	15.6 ± 1.7	31.3 ± 4.1	5.8 ± 0.6	9.2 ± 0.8
M5-A4-0309[d]	SiC	X1	0.8	1690.3 ± 108.4	35.9 ± 0.5	−342 ± 12	−606 ± 8	0.72 ± 0.05	15.4 ± 1.7	45.8 ± 6.0	6.6 ± 0.8	11.9 ± 1.0
M5-A4-0322-2	SiC	X1	1.8	68.8 ± 1.2	54.2 ± 0.7	−301 ± 7	−418 ± 5	1.07 ± 0.07	9.9 ± 1.1	19.8 ± 2.6	6.3 ± 0.6	9.2 ± 0.8
M5-A4-0361	SiC	X1	1.0	179.4 ± 4.0	75.0 ± 1.0	−242 ± 14	−414 ± 10	0.82 ± 0.05	17.5 ± 1.9	45.6 ± 6.0	30.6 ± 1.2	44.9 ± 1.5
M5-A4-0691	SiC	X1	1.1	322.3 ± 8.5	45.2 ± 0.6	−308 ± 12	−434 ± 10	0.79 ± 0.05	10.2 ± 1.1	27.8 ± 3.7	9.5 ± 1.0	13.4 ± 1.0
M5-A5-0071	SiC	X1	2.4	818.3 ± 25.2	42.1 ± 0.6	−340 ± 14	−626 ± 5	0.85 ± 0.05	7.9 ± 0.8	19.8 ± 2.6	11.7 ± 4.6	9.1 ± 3.7
M5-A5-2856[d]	SiC	X2	1.0	143.7 ± 2.7	39.0 ± 0.5	−498 ± 9	−611 ± 7	0.87 ± 0.06	39.8 ± 4.3	97.6 ± 12.8	30.2 ± 13.2	31.3 ± 13.9
M5-A6-1154	Si_3N_4	X1	0.8	87.6 ± 3.1	39.5 ± 0.8	−374 ± 3	−536 ± 4	0.96 ± 0.02	3.4 ± 0.4	6.2 ± 0.5	15.4 ± 1.7	38.4 ± 2.3
M5-A7-0303	SiC	X2	1.0	878.8 ± 25.8	72.0 ± 1.0	−480 ± 9	−370 ± 9	0.98 ± 0.06	7.6 ± 0.8	16.6 ± 2.2	3.7 ± 0.8	4.8 ± 0.8
M5-A7-0663	SiC	X1	1.0	656.6 ± 19.0	34.7 ± 0.5	−498 ± 9	−690 ± 5	1.03 ± 0.07	5.1 ± 0.6	10.6 ± 1.4	5.7 ± 0.9	8.9 ± 0.9
M5-A7-1003	SiC	X1	0.8	338.4 ± 8.5	46.4 ± 0.7	−320 ± 12	−446 ± 9	0.83 ± 0.05	7.7 ± 0.8	20.0 ± 2.6	3.5 ± 1.0	29.2 ± 1.4
M5-A7-1613[d]	SiC	X1	1.1	37.0 ± 0.6	42.3 ± 0.5	−173 ± 14	−212 ± 12	0.47 ± 0.03	8.1 ± 0.9	37.0 ± 4.9	4.4 ± 1.0	10.6 ± 1.3
M5-A7-2335[d]	SiC	X1	1.8	243.0 ± 4.8	12.7 ± 0.2	−171 ± 14	−229 ± 11	1.03 ± 0.08	0.5 ± 0.1	0.9 ± 0.1	N.D.[e]	N.D.
M5-A7-2884[d]	SiC	X1	1.9	4862.0 ± 182.4	31.0 ± 0.4	−475 ± 9	−709 ± 4	1.21 ± 0.08	3.6 ± 0.4	6.4 ± 0.8	3.3 ± 0.5	5.2 ± 0.5
M5-A7-2897	SiC	X2	0.5	1212.3 ± 36.2	31.1 ± 0.2	−512 ± 8	−453 ± 8	0.74 ± 0.05	3.8 ± 0.4	11.1 ± 1.5	3.7 ± 0.8	6.5 ± 1.0
M6-A1-0228[d]	SiC	X1	0.6	30.8 ± 0.2	33.9 ± 0.8	−141 ± 7	−175 ± 9	0.74 ± 0.05	28.8 ± 3.1	77.9 ± 6.0	22.1 ± 1.9	178.4 ± 2.9
M6-A1-4635	SiC	X1	0.8	22.8 ± 0.1	21.5 ± 0.5	−268 ± 6	−347 ± 7	0.79 ± 0.05	12.4 ± 1.4	31.3 ± 2.4	22.1 ± 1.7	117.0 ± 2.2
M6-A1-5959[d]	SiC	X1	0.5	120.1 ± 1.2	62.0 ± 1.4	−246 ± 5	−408 ± 6	0.68 ± 0.01	10.9 ± 1.2	28.3 ± 2.2	3.9 ± 1.8	6.4 ± 2.2
M6-A2-0222[d]	SiC	X1	1.2	140.9 ± 1.1	68.3 ± 1.6	−280 ± 3	−495 ± 4	0.75 ± 0.02	2.9 ± 0.3	6.8 ± 0.5	1.8 ± 0.9	3.9 ± 0.9
M6-A3-0852	SiC	X1	01.0	144.4 ± 2.2	129.7 ± 4.7	−278 ± 10	−422 ± 10	0.60 ± 0.04	8.6 ± 0.9	28.7 ± 2.2	5.8 ± 1.2	10.5 ± 1.2
M6-A3-0983	Si_3N_4	X1	1.0	35.5 ± 2.4	53.0 ± 2.0	−152 ± 5	−253 ± 5	0.89 ± 0.06	3.9 ± 0.4	8.7 ± 0.7	N.D.	9.5 ± 1.4
M6-A3-1169[d]	SiC	X1	0.7	291.1 ± 6.6	51.3 ± 1.7	−335 ± 6	−593 ± 6	1.00 ± 0.07	5.3 ± 0.6	10.6 ± 0.9	8.0 ± 1.4	12.9 ± 1.7
M6-A3-1802[d]	SiC	X2	0.5	1755.5 ± 118.8	66.6 ± 3.1	−652 ± 7	−568 ± 10	0.76 ± 0.06	10.4 ± 1.2	27.2 ± 2.2	8.3 ± 1.3	11.4 ± 1.6
M6-A4-0151[d]	SiC	X1	0.8	627.0 ± 13.4	20.5 ± 0.5	−351 ± 6	−488 ± 6	0.64 ± 0.05	4.6 ± 0.5	14.4 ± 1.2	5.5 ± 1.5	14.8 ± 2.0
M6-A5-0243	SiC	X2	0.7	2974.7 ± 151.7	68.4 ± 2.6	−582 ± 5	−475 ± 6	0.98 ± 0.07	4.1 ± 0.4	8.3 ± 0.6	4.7 ± 1.0	22.0 ± 0.5
M6-A5-1485	SiC	X1	1.0	406.5 ± 12.3	67.6 ± 2.5	−321 ± 6	−458 ± 7	1.16 ± 0.08	11.6 ± 1.3	19.9 ± 1.6	12.8 ± 1.1	70.5 ± 1.1
M6-A5-1858	SiC	X1	0.9	191.2 ± 2.4	118.2 ± 4.3	−377 ± 4	−567 ± 4	0.67 ± 0.05	2.8 ± 0.3	8.4 ± 0.7	4.1 ± 0.9	31.1 ± 0.5
M6-A6-0109	SiC	X2	1.0	377.7 ± 7.9	135.2 ± 4.8	−465 ± 6	−345 ± 7	0.59 ± 0.04	12.2 ± 1.3	41.3 ± 3.2	10.7 ± 1.6	64.1 ± 0.9
M6-A6-1330	Si_3N_4	X0	1.0	99.2 ± 8.5	39.0 ± 1.0	−332 ± 5	−648 ± 4	1.41 ± 0.10	1.9 ± 0.2	2.6 ± 0.2	3.7 ± 1.7	N.D.
M6-A6-3269	Si_3N_4	X0	0.5	185.8 ± 83.5	20.2 ± 0.5	−98 ± 9	−305 ± 9	0.56 ± 0.05	1.6 ± 0.2	5.9 ± 0.5	7.1 ± 3.3	11.1 ± 3.3
M6-A7-0883	SiC	X1	0.7	503.2 ± 12.9	28.5 ± 0.5	−399 ± 6	−515 ± 7	0.88 ± 0.02	87.4 ± 9.5	173.9 ± 13.5	31.5 ± 1.7	39.1 ± 1.8
M6-A7-2790-2	SiC	X1	0.5	173.4 ± 2.5	71.6 ± 1.2	−215 ± 7	−377 ± 7	0.69 ± 0.05	24.8 ± 2.7	72.4 ± 5.6	2.7 ± 0.8	2.2 ± 0.8
M6-A7-3156[d]	SiC	X0	0.6	107.7 ± 1.2	35.5 ± 0.6	240 ± 7	−161 ± 6	0.32 ± 0.03	1.3 ± 0.1	8.0 ± 0.6	2.6 ± 1.3	7.6 ± 1.4
M6-A7-3184[d]	SiC	X2	0.8	2411.7 ± 88.3	4.0 ± 0.1	−492 ± 4	−269 ± 6	0.53 ± 0.01	20.3 ± 2.2	67.9 ± 5.3	12.2 ± 1.3	18.9 ± 1.5

Notes.
[a] $\delta^i Si_{28}$ was calculated using the equation $\delta^i Si_{28} = [(^iSi/^{28}Si)_{grain} / (^iSi/^{28}Si)_{std} - 1] \times 1000$, in which ^{i}Si denotes ^{29}Si or ^{30}Si.
[b] The initial $^{26}Al/^{27}Al$ ratios were calculated by adopting the $\Gamma_{Mg/Al}$ value (0.69) inferred in Section 3.1. The associated errors are based on counting statistics and uncertainties in $\Gamma_{Mg/Al}$ determined from Burma spinel measurements.
[c] The associated errors are based on counting statistics and uncertainties in $\Gamma_{Mg/Si}$ and $\Gamma_{Al/Si}$ values determined from NIST 610 measurements.
[d] This X grain had relatively uniform ^{26}Mg and was thus included in Figure 2(a) to derive $\Gamma_{Mg/Si}$ value.
[e] N.D. stands for not detected.

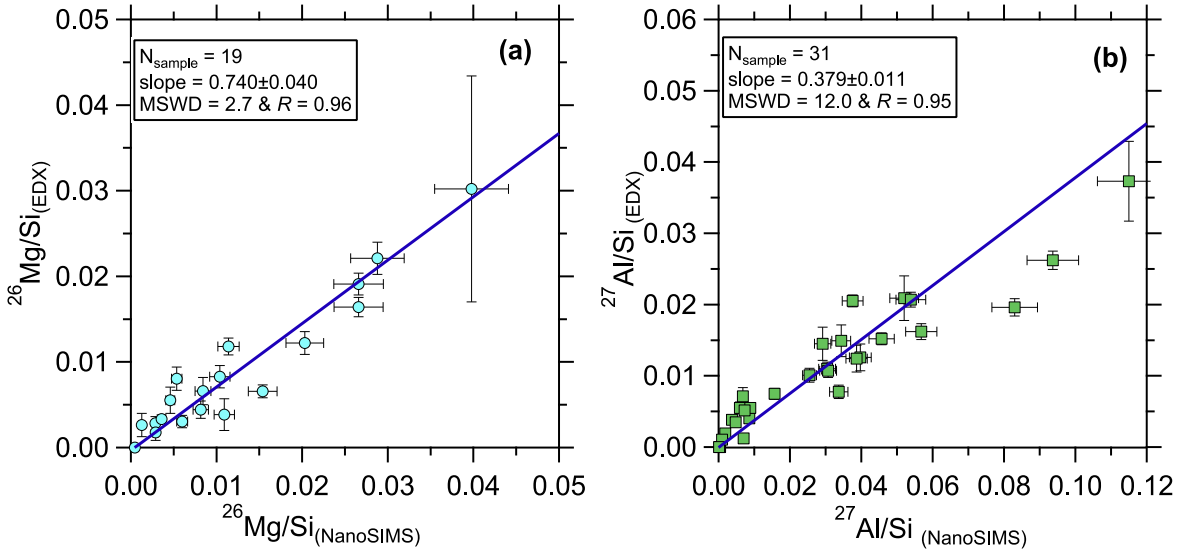

Figure 2. Plots comparing BSE-EDX and NanoSIMS results for X SiC (panel (a)) and mainstream SiC (panel (b)) grains. The linear fits to the grain data are plotted as solid blue lines, and the corresponding slopes are given in each panel. Errors are all 1σ. The NanoSIMS data were calculated by adopting $\Gamma_{Mg/Si}$ and $\Gamma_{Al/Si}$ values of 5.31 and 3.96, respectively. The linear fits were obtained using the CEREsFit.xlsm tool of Stephan & Trappitsch (2023). MSWD stands for mean squared weighted deviation, and R is the Pearson correlation coefficient.

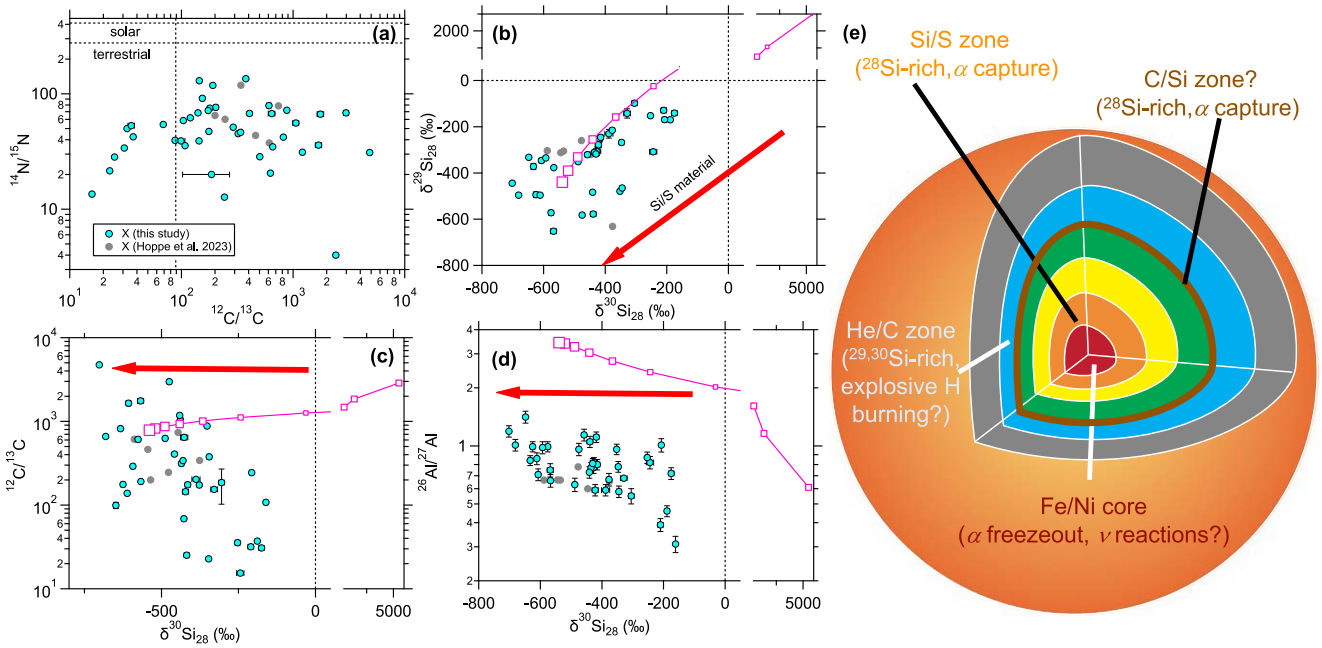

Figure 3. Panels (a)–(d) compare CCSN grain data from this study and Hoppe et al. (2023) with our CCSN nucleosynthesis calculations. The average composition of the Fe/Ni core was calculated by mixing Fe/Ni material from the ν- and no-ν-models with a mixing ratio of 3:2, respectively, and the calculated average compositions at explosion energies of (1–10) × 10^{51} erg are plotted as squares (increasing size with increasing E) with lines. In panel (a), the model calculations are out of scale (see discussion in Section 3.2.4). The effects of mixing with ^{28}Si-rich Si/S material are illustrated using red arrows. In panel (e), shown is a schematic diagram of the "onion-shell" internal structure of a presupernova massive star.

in Figure 2(b) than in Figure 2(a), other parameters such as Al contamination probably caused the larger scatter of the grain data in Figure 2(b).

For future studies of Al–Mg isotopes in presolar SiC grains, we recommend measuring polished NIST glass and Burma spinel standards for comparison with this study, based on which our derived $\Gamma_{Mg/Al}$ value can be applied for their initial $^{26}Al/^{27}Al$ calculations. Due to the lack of proper Si_3N_4 standards, we also adopted $\Gamma_{Mg/Al} = 0.69$ for deriving the initial $^{26}Al/^{27}Al$ ratios of the four Si_3N_4 grains. This is because the O abundance likely controls $\Gamma_{Mg/Al}$ (see Appendix A for discussion) and SiC and Si_3N_4 are both O-free. Figure A7 shows that the derived initial $^{26}Al/^{27}Al$ ratios of the Si_3N_4 grains generally follow the trend defined by X SiC grain data.

3.2. Comparison with CCSN Nucleosynthesis Models

3.2.1. Lack of C, N, and Al Isotopic Differences between X1 and X2 Grains

Figure 3 shows that our CCSN grains span wide ranges of C, N, and Si isotopic compositions, but their initial $^{26}Al/^{27}Al$ ratios vary only from 0.3 to 1.4, in contrast to the wide range

(~0.01–0.5) observed previously (Stephan et al. 2021). Given the lowered $\Gamma_{Mg/Al}$ in SiC and observed Al contamination in this study, we suggest that the inappropriate calibration of $\Gamma_{Mg/Al}$ in previous studies caused their low upper limit[9] and that the varying degrees of Al contamination sampled in previous studies caused their wide range of initial $^{26}Al/^{27}Al$ ratios. With this new set of CCSN grain data, we observed negative trends between $^{12}C/^{13}C$ and $\delta^{30}Si_{28}$ and between $^{26}Al/^{27}Al$ and $\delta^{30}Si_{28}$ (Figures 3(c), (d)) that are further supported by the CCSN grain data from Hoppe et al. (2023). These isotope trends are in line with the negative trends for $^{44}Ti/^{48}Ti$–$\delta^{29}Si_{28}$ (Lin et al. 2010) and $^{49}Ti/^{48}Ti$–$\delta^{30}Si_{28}$ values (Liu et al. 2018a).

Based on Si isotope ratios, Lin et al. (2010) proposed dividing X grains into subtypes X0, X1, and X2 grains. We, however, observed no substantial differences in $^{12}C/^{13}C$, $^{14}N/^{15}N$, and initial $^{26}Al/^{27}Al$ ratios between our X1 and X2 grains (see Figure A7 in Appendix B). In comparison, Stephan et al. (2018) identified low $^{87}Sr/^{86}Sr$ and $^{88}Sr/^{86}Sr$ values in two X2 grains that differ significantly from those of X1 grains, and Liu et al. (2023) reported a significantly larger ^{48}Ti enrichment in one X2 grain than in X1 grains. Given the limited statistics, it is still questionable whether the subtype classification scheme is appropriate. We will, therefore, discuss the X grain data without the subtype classification.

3.2.2. Underproduction of ^{26}Al in C/Si Zone and Explosive H Burning in He Shell

That the majority of CCSN grains fall along a line in Figure 3(b) points to two-end-member mixing, which suggests that CCSN grains sampled materials mainly from the innermost CCSN zones that were enriched in α isotopes (e.g., ^{28}Si) and outer zones, i.e., the He/C zone and zones above it, that are relatively more enriched in ^{29}Si and ^{30}Si (Figure 3(e)). Alternatively, Pignatari et al. (2013) ascribed the ^{28}Si enrichments of CCSN grains to materials from the C/Si zone in high-explosion-energy CCSNe (Figure 3(e)), where the high temperatures ($T > 3.5 \times 10^8$ K) enable a chain of α-capture reactions. Compared to the inner-zone scenario, the C/Si scenario requires only relatively small-scale, local mixing to reproduce CSSN grain compositions and avoids the problem of selective mixing of materials on large scales required by the former (Figure 3(e)). In addition, Pignatari et al. (2015) proposed that the entire He shell could retain up to percent-level H mixed inward from the surface H-rich envelope until the explosion, producing copious ^{13}C, ^{15}N, and ^{26}Al by proton-capture reactions in the He/C zone during the explosion. The explosive H burning scenario greatly lowers $^{12}C/^{13}C$ and $^{14}N/^{15}N$ ratios and enhances $^{26}Al/^{27}Al$ ratios in the He/C zone.

The isotope trend in Figure 3(c) supports the occurrence of explosive H burning in the He shell, given that the trend points to quite low $^{12}C/^{13}C$ ratios (<10–100) for the ^{30}Si-rich end-member. It is, however, debatable whether the explosive H burning process occurred in the He/C zone as proposed by Pignatari et al. (2015) and/or in the He/N zone as shown in Liu et al. (2018b). In fact, the inferred composition of the ^{30}Si-rich end-member is comparable to those of the He/N zone at varying E as reported in Liu et al. (2018b).

The isotope trend in Figure 3(d) suggests that the ^{28}Si-rich end-member tends to produce higher $^{26}Al/^{27}Al$ ratios (>2) than the ^{30}Si-rich end-member. The ^{28}Si-rich C/Si zone in the models of Pignatari et al. (2015) and Schofield et al. (2022), however, have been shown to produce $^{26}Al/^{27}Al$ ratios that are significantly below one. Although Hoppe et al. (2023) could reproduce their X grain isotopic compositions by invoking the C/Si and explosive H burning scenarios based on the models of Pignatari et al. (2015), the explosive H burning zone (^{30}Si-rich) produces higher $^{26}Al/^{27}Al$ ratios than the C/Si zone (^{28}Si-rich, Figure 3(e)), which consequently implies a positive trend between $^{26}Al/^{27}Al$ and $\delta^{30}Si_{28}$ that contradicts the negative trend observed in Figure 3(d). This contradiction reflects limitations and uncertainties in the ad hoc mixing calculations. Moreover, none of our nucleosynthesis calculations yielded a C/Si zone in the outer region, even though the He/C zone achieves up to 1×10^9 K at $E = 10 \times 10^{51}$ erg, thus suggesting that high temperature is not the only necessary ingredient for producing the C/Si zone. Given the strong model dependence, it is highly uncertain as to whether a C/Si zone exists in CCSNe.

3.2.3. Evidence for Neutrino Reactions in CCSNe

Figure 4 illustrates that neutrino reactions significantly enhance the production ratio of $^{26}Al/^{27}Al$ in the Fe/Ni core but not in the Si/S zone, which is found in our CCSN models at all explosion energies. This observation points out that the enhanced production of $^{26}Al/^{27}Al$ requires both the presence of neutrinos and an α-rich freeze-out from quasi-equilibrium (see Meyer et al. 1998a for details). Neutrino–nucleus reactions during the α-rich freeze-out maintain a relatively high abundance of free protons. Proton-capture reactions then enhance the production of ^{26}Al over the freeze-out without neutrino–nucleus interactions. A detailed comparison of the CCSN grain data from this study with the ν-model calculations for the Fe/Ni core is shown in Figure A8. Figure A8 illustrates that the CCSN grain data link high initial $^{26}Al/^{27}Al$ ratios (>2) to the ^{28}Si-rich end-member, in line with the high $^{26}Al/^{27}Al$ ratios predicted by the ν-models for the Fe/Ni core at $E > 2 \times 10^{51}$ erg. Thus, the Fe/Ni core likely contributed to the CCSN ejecta from which the CCSN grains condensed.

We further illustrated the effect of mixing additional material from the adjacent Si/S zone in Figure A8. This is because the Fe/Ni core contains pure ^{48}Ti and cannot account for the large ^{49}Ti excesses observed in X grains, which require contributions from the Si/S zone (Liu et al. 2018a). Given the copious production of pure ^{28}Si in the Si/S zone, this additional mixing results in simultaneous reduction in $^{29}Si/^{28}Si$ and $^{30}Si/^{28}Si$ with negligible effects on the other isotope ratios (for reproducing the isotopic compositions of CCSN grains). Thus, the composition of the mixed Fe/Ni and Si/S ejecta would approach $\delta^{30}Si_{28} = -1000‰$ along a slope-1 line in the Si 3-isotope plot by mixing with Si/S zonal material. This mixed ejecta that consists of materials from both the Fe/Ni core and Si/S zone, provide a natural explanation as to why CCSN grains data do not fall along a slope-1 line (Figure A8(b)) if the Si/S zone with pure ^{28}Si is one of the two end-members.

This large-scale mixing between innermost CCSN material with outer C-rich material is supported by the observations that ^{56}Ni and ^{44}Ti knots in CCSN remnants are inside out, i.e., lie

[9] Hoppe et al. (2023) adopted a $\Gamma_{Mg/Al}$ value that is half of the value determined based on their polished NIST 611 glass measurements. Their adopted $\Gamma_{Mg/Al}$ value is thus consistent with the value derived in Section 3.1, and their X grain data can be directly compared to our data as shown in Figure 3.

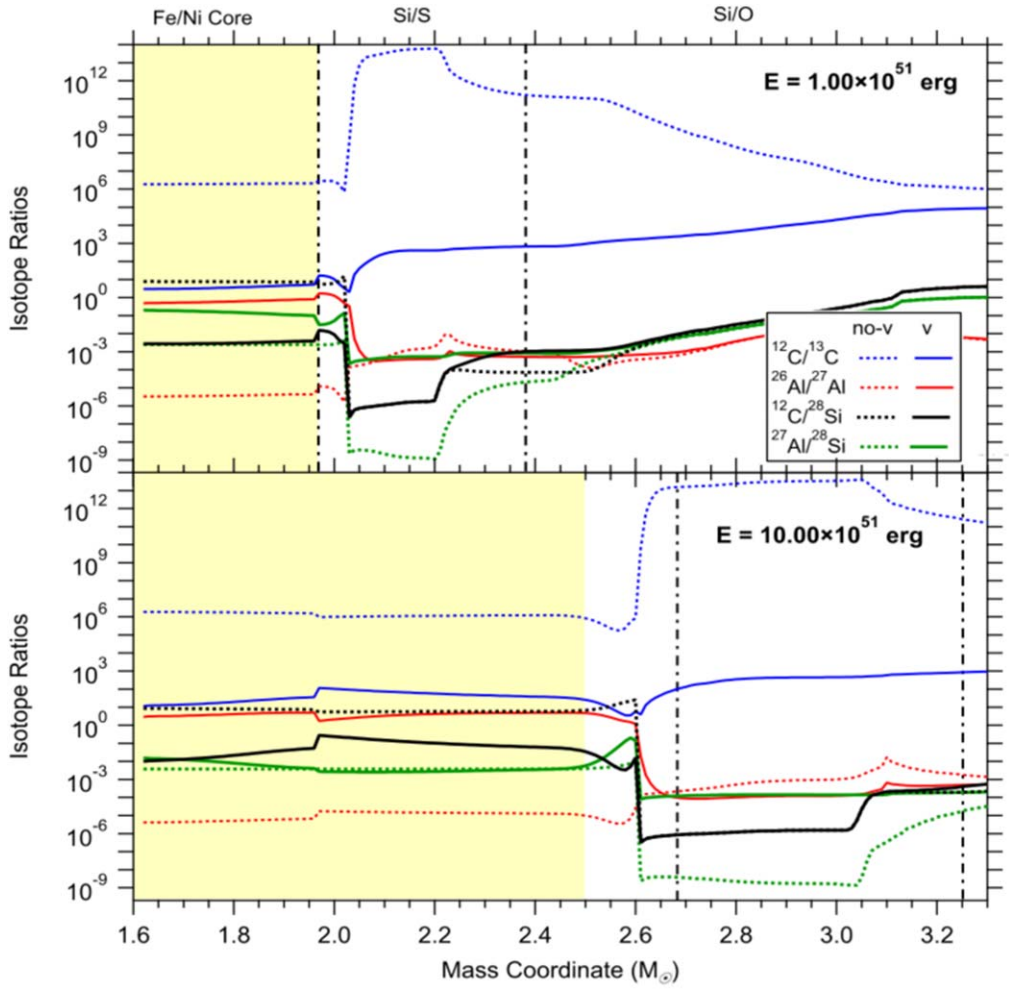

Figure 4. Comparison of the ν- and no-ν-models in deep CCSN regions at the lowest and highest considered explosion energies. In the Fe/Ni core, CCSN layers with relatively homogenous compositions are chosen for calculating the average compositions (highlighted in yellow) that are shown as magenta squares in Figures 3 and A8.

outside the central regions of CCSN remnants (e.g., Hwang & Laming 2012). The observed ^{56}Ni and ^{44}Ti were inferred to have been assembled under α-rich freeze-out, corresponding to the Fe/Ni core material (Wongwathanarat et al. 2017). Furthermore, based on three-dimensional model simulations, the restricted mixing of Fe/Ni and Si/S materials with those from the outer He/C zone (and zones above it), is suggested to be a natural consequence of shock deceleration in the He shell and consequent pileup of metal-rich knots from the interior in the He shell (Hammer et al. 2010; Wongwathanarat et al. 2017). The simulations further predict that Rayleigh–Taylor instabilities could develop at the H/He interface and eventually lead to metals and He being mixed into the H envelope, in line with the suggestions from CCSN grain data (e.g., Xu et al. 2015).

3.2.4. The Problem of $^{12}C/^{13}C$

In contrast to the high ^{12}C/^{13}C value of >1000–10,000 inferred for the ^{28}Si-rich end-member (Figure A8(c)), ^{12}C/^{13}C is predicted to lie below 100 in the Fe/Ni core in the presence of neutrino reactions as shown in Figure A8(c). In a proton-rich condition, ^{13}C and ^{26}Al are generally predicted to be abundantly produced together at different stellar sites (e.g., nova explosions; José et al. 2004). Therefore, the high ^{12}C/^{13}C and ^{26}Al/^{27}Al ratios inferred for the ^{28}Si-rich end-member seem counterintuitive. Core-collapse explosions, however, are complex phenomenon that are in great contrast to other stellar environments as, for instance, α-rich freeze-outs occur solely in CCSNe. Specifically, ^{12}C is a product of α-rich freeze-outs, and ^{13}C is made abundantly in the proton-rich condition created by neutrino–nucleus reactions. Thus, the data-model discrepancy for ^{12}C/^{13}C could imply, for instance, uncertainties in the calculation of α-rich freeze-outs. Beside uncertainties in nucleosynthesis calculations, below we explore one scenario to enhance the high ^{12}C/^{13}C ratio of the core that involves mixing core materials experiencing varying proton fluxes.

It is conceivable that in the Fe/Ni core materials are contained in different bubbles that could encounter different neutrino fluxes and mixing occurs between materials that experience strong and weak proton fluxes. Although the model predictions for the ^{12}C/^{13}C ratio in the core is not sensitive to the neutrino flux across a wide range based on our model tests, the Fe/Ni core is predicted to contain almost pure ^{12}C in the absence of neutrino reactions (Figure 4). In addition, three-dimensional hydrodynamic model simulations predict that the Fe/Ni core material penetrates into the He shell at different rates (e.g., Hwang & Laming 2012), which means that the Fe/Ni material probably left the deep core region at different times so that some of the fast-moving core material may not have time to experience

the neutrino-reaction-induced proton flux, corresponding to the no-ν scenario. Also, three-dimensional hydrodynamic models predict the most fast-moving core material to have the highest likelihood to penetrate into the He shell (e.g., Hwang & Laming 2012), the condition inferred for producing the SiC and Si_3N_4 grains from our study.

As a test, we mixed Fe/Ni core material from the ν- and no-ν-model with a mixing ratio of 3:2, respectively. Our test revealed that such mixing could lead to significant increases in $^{12}C/^{13}C$ with much smaller effects on the other isotope ratios in Figure 3, thus accounting for the large ^{12}C ($^{12}C/^{13}C > 1000$–10,000) and ^{26}Al ($^{26}Al/^{27}Al > 2$) enrichments in the ^{28}Si-rich end-member. The predicted compositions at varying E based on this mixing scenario are shown in Figure 3 for comparison with the grain data. The predicted $^{14}N/^{15}N$ for the Fe/Ni core increases from 0.06 to 1.00 with increasing E, all of which, however, are very low with respect to the CCSN grain data and are thus not shown in Figure 3(a). Given the lack of any trend observed between $^{14}N/^{15}N$ and $^{30}Si/^{28}Si$, we cannot derive any constraints on the $^{14}N/^{15}N$ ratio of the ^{28}Si-rich end-member, which thus precludes data-model comparisons in a similar way as for the other isotope systematics. In addition, the $^{14}N/^{15}N$ ratio of the Fe/Ni core is affected by the radioactive decay of ^{14}C ($t_{1/2} = 5730$ a), and the relative ratio of $^{14}C/^{14}N$ that was initially incorporated into CCSN grains remains poorly constrained. Nevertheless, a positive trend between $^{12}C/^{13}C$ and $^{14}N/^{15}N$ ratios seems to exist among CCSN grains with subsolar carbon isotope ratios, likely pointing to coproduction of ^{13}C and ^{15}N in the He shell by explosive H burning.

4. Conclusions

The correlated isotopic and elemental data of X grains from this study enabled accurate determination of their initial $^{26}Al/^{27}Al$ ratios. Our new grain data suggest that the Al/Mg ratios in SiC are a factor of 2 lower than estimated based on the SIMS analyses that used O-rich standards, corresponding to a factor of 2 increase in the derived initial $^{26}Al/^{27}Al$ ratios for presolar SiC grains. For future studies of Al–Mg isotopes in presolar SiC grains, we recommend measuring polished NIST glass and Burma spinel standards for comparison with this study, based on which our derived $\Gamma_{Mg/Al}$ value can be applied for their initial $^{26}Al/^{27}Al$ calculations.

For the first time, we observed negative trends for $^{12}C/^{13}C$–$\delta^{30}Si_{28}$ and $^{26}Al/^{27}Al$–$\delta^{30}Si_{28}$ among CCSN grains, which are in line with the negative trends for $^{44}Ti/^{48}Ti$–$\delta^{29}Si_{28}$ and $^{49}Ti/^{48}Ti$–$\delta^{30}Si_{28}$ reported in the literature. These isotope trends corroborate the two-end-member (^{28}Si-rich and ^{30}Si-rich) mixing scenario suggested by the Si isotopic compositions of CCSN grains. The isotope trends from this study suggest lower ^{13}C and higher ^{26}Al enrichments in the ^{28}Si-rich end-member, and higher ^{13}C and lower ^{26}Al enrichments in the ^{30}Si-rich end-member.

The CCSN grain data do not support previous suggestions that the C/Si zone is the source of the ^{28}Si-rich end-member, given that current CCSN stellar nucleosynthesis models all underproduce ^{26}Al in this zone. Instead, the grain data favor mixtures of the innermost CCSN Fe/Ni and Si/S zones as the ^{28}Si-rich end-member. Our model calculations further illustrate that, during α-rich freeze-out in the presence of neutrinos, a proton-rich condition could be created in the core, leading to abundant ^{26}Al production and thus accounting for the high $^{26}Al/^{27}Al$ ratios inferred for the ^{28}Si-rich end-member. However, the models predict $^{12}C/^{13}C$ ratios that are lower than inferred from the grain data for the Fe/Ni core. The data-model discrepancy could be reconciled if the core material that penetrated into the He shell experienced a wide range of neutrino fluxes.

The ^{30}Si-rich end-member is most likely a mixture of He- and H-shell material. The grain data also suggest that explosive H burning must have occurred in the He shell to produce the low $^{12}C/^{13}C$ and $^{14}N/^{15}N$ ratios of the ^{30}Si-rich end-member. The exact location for the explosive H burning, however, is unclear, and both the He/C and He/N zones within the He shell remain potential candidates.

The large-scale mixing of innermost CCSN material with outer He- and H-shell materials, is in line with astronomical observations and three-dimensional model simulations. However, our conclusions, which are based on C, Al–Mg, and Si isotope ratios and one-dimensional model calculations, need to be tested by including analyses of more isotope systematics in CCSN grains and considering state-of-the-art multidimensional CCSN simulations (e.g., Sandoval et al. 2021) and their nucleosynthesis yields (e.g., Sieverding et al. 2023).

Acknowledgments

This work was supported by NASA through grants 80NSSC20K0387 to N.L., NNX10AI63G and NNX17AE28G to L.R.N, 80NSSC20K0338 to B.S.M, and 80NSSC23K0011 to R.M.S. CASINO simulations used the CASINO V2.51 software made available by the University of Sherbrooke, Montreal Canada.

Supplementary Material

Appendix A

A.1. Mg/Si and Al/Si Ratios of Presolar SiC Grains

We performed CASINO simulations for 10,000 electrons in a 5 nm, 1 nA, 10 kV beam incident on an infinite slab of $Si_{48}C_{48}AlMg_3$, with a density of 3.31 g cm^{-3}. The CASINO simulation in Figure A1 reveals nearly identical Mg, Al, and Si X-ray yield depth distribution profiles. This indicates that the X-ray yield is not appreciably affected by differential absorption, and elemental quantification using PhiRhoZ methods are valid despite the particle morphology, i.e., Mg/Si and Al/Si values are insensitive to variations in detector position or SiC particle morphology. Furthermore, the electron interaction volume (Figure A1 inset) illustrated by 1000 of the 10,000 simulated trajectories (blue lines) is $\sim$1 μm^2 in lateral range and 0.8 μm in depth, which indicates that the X-ray signal samples a representative, subsurface volume of the particle for most particle sizes in this study (0.5–1 μm in diameter).

Figure A2(a) shows that the correlation between EDX- and NanoSIMS-derived $^{26}Mg/Si$ ratios determined based on the full set of our X grain data (0.89 ± 0.03, 1σ error) agrees with that determined based on the 19 selected X grains (relatively chemically homogenous) in Figure 2(a) (0.74 ± 0.04) within 2σ uncertainties. The larger MSWD along with the smaller R values in the former are, therefore, likely caused by the heterogenous distributions of Al and thus ^{26}Mg in 20 of the 39 X grains, which must have led to sampling materials with

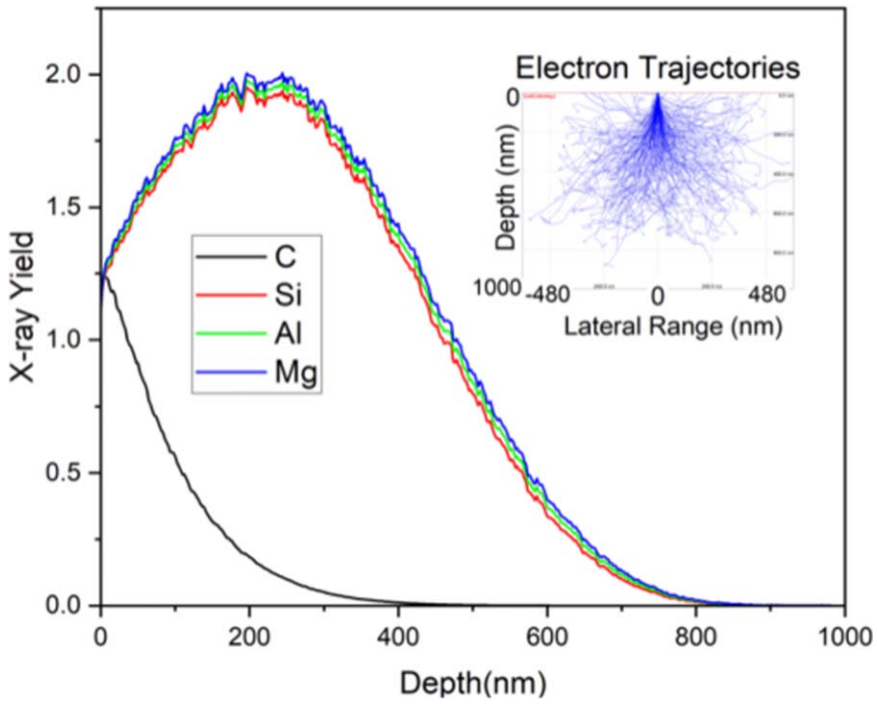

Figure A1. CASINO simulation (Drouin et al. 2007) of characteristic X-ray yields (C, Si, Al, and Mg K peaks) and electron trajectories for a 1 nA, 10 kV beam of 5 nm in size incident on an infinite slab of $Si_{48}C_{48}AlMg_3$. In the inset, blue trajectories represent 1000 of the 10,000 calculated electron trajectories within the slab. The electron trajectory distribution spans a ~0.8 μm diameter teardrop-shaped interaction volume, comparable in size to the average grain diameter in this study.

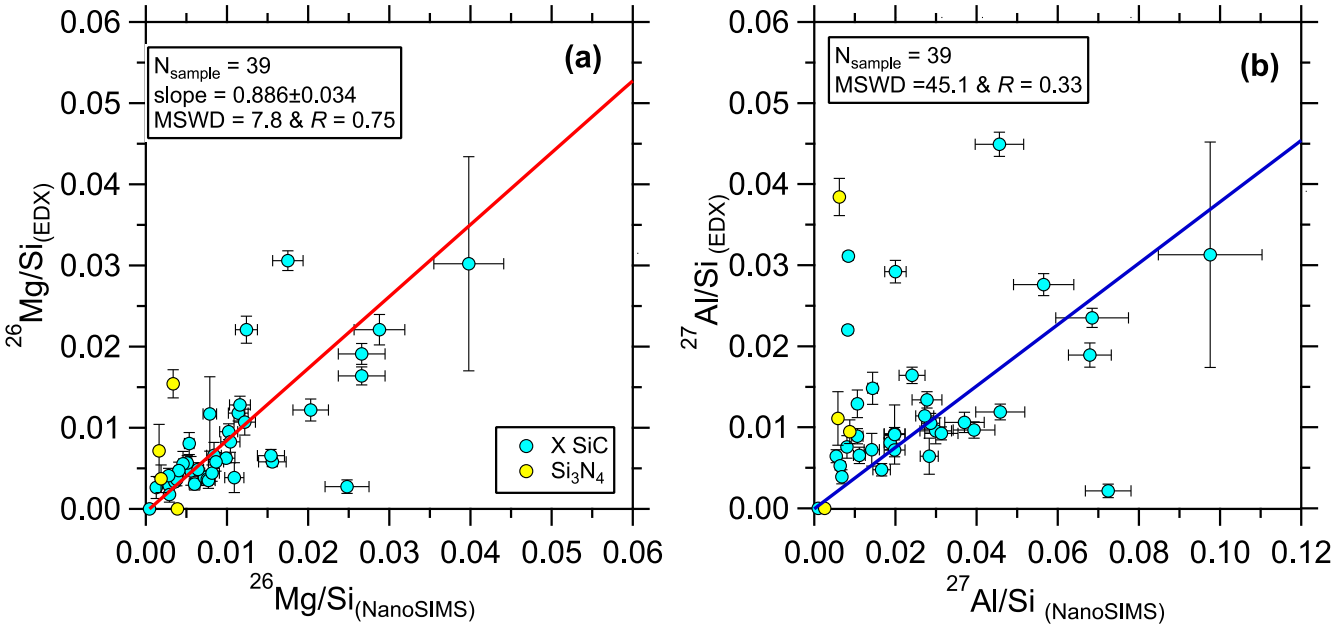

Figure A2. Plots comparing BSE-EDX and NanoSIMS analysis results of all X grains from this study. In panel (a), the linear fit to the grain data is plotted as a solid red line and was obtained by using the CEREsFit.xlsm tool of Stephan & Trappitsch (2023). In panel (b), given the small R value, we did not obtain any linear fit to the grain data and instead plotted the linear fit to the selected MS grain data in Figure 2(b) for comparison. Data for Si_3N_4 grains are plotted for comparison. Errors are all 1σ.

varying ^{26}Mg/Si ratios from each of these grains by coordinated EDX and NanoSIMS analyses. The 39 X grains are also much less well correlated for Al/Si in Figure A2(b) than for Mg/Si in Figure A2(a), given the significantly enlarged MSWD and reduced R values of the former. The differences likely result predominantly from the effects of Al contamination on EDX-derived Al/Si ratios.

Figure A3(a) further illustrates that 126 MS grains from this study are better correlated than the 39 X grains in Figure A2(b) between their EDX- and NanoSIMS-derived Al/Si ratios. The better correlated grain data in the former likely result from the suppressed effects of Al contamination on their EDX data because of their enlarged sizes (Figure A3(b)) and, in turn, increased volume-to-rim ratios (since Al contaminations

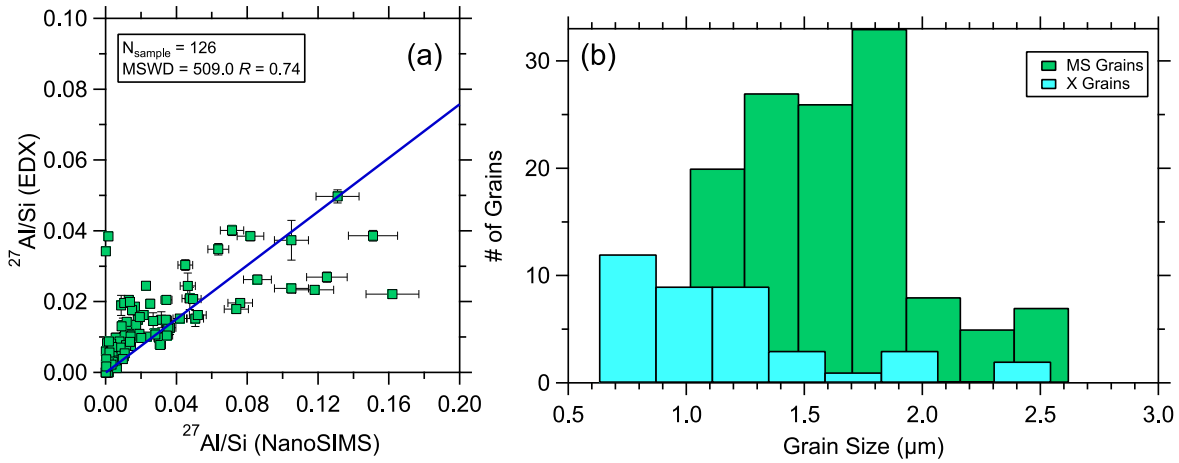

Figure A3. The plot in panel (a) is the same as Figure A2(b) but for 126 MS grains. In panel (b), MS grains from panel (a) are compared to X grains in Figure A2 for their grain size distributions.

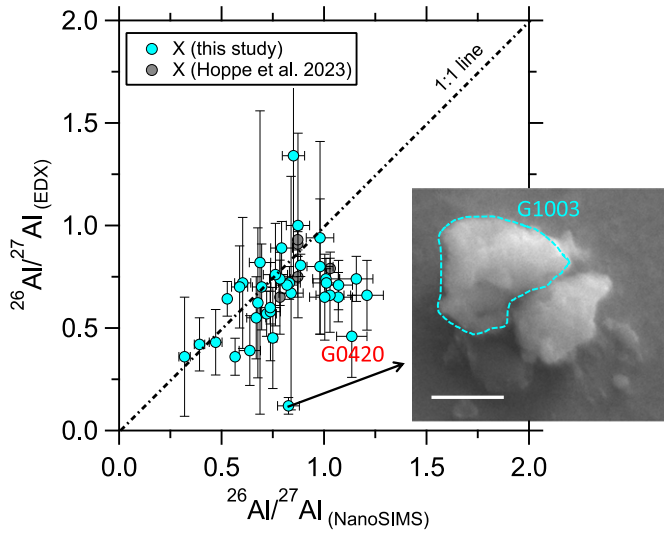

Figure A4. EDX- and NanoSIMS-derived initial $^{26}Al/^{27}Al$ ratios of X grains from this study and Hoppe et al. (2023). Labeled is grain M5-A3-0420 that had significant Al contamination (Figure 1). In the insert, the SEM image of grain M5-A7-1003 shows that this X grain was part of a SiC aggregate so that the adjacent SiC, which is an MS grain with $^{26}Al/^{27}Al = 0.001$, significantly lowered its EDX-derived Mg content and, in turn, $^{26}Al/^{27}Al$ ratio. The scale bar denotes 500 nm.

mainly appear as rims, e.g., grain 0420 in Figure 1). Compared to Figure 2(b), the enlarged MSWD and reduced R values in Figure A3(a) are likely caused by (i) sampling materials with varying Al/Si ratios by EDX and NanoSIMS analyses, given that the grains are scattered both below and above the linear fit and/or (ii) sampling higher levels of Al contamination by EDX analyses, given that a significant fraction of the MS grains lie above the linear fit.

Figure A4 compares the initial $^{26}Al/^{27}Al$ ratios derived based on EDX and NanoSIMS analyses. A significant fraction of the X grains from this study and Hoppe et al. (2023) are scattered around 1:1 line within 1σ uncertainties, thus corroborating our derived $\Gamma_{Mg/Al}$ (0.69 ± 0.04) value in SiC. That several X grains lie significantly below the 1:1 line, is most likely caused by (i) the significant amounts of Al contamination sampled by their EDX analyses (e.g., grain M5-A3-0420, Figure1) and/or (ii) dilution from adjacent grains in the EDX data due to grain aggregation (grain M5-A7-1003, Figure A4).

A.2. New $\Gamma_{Mg/Al}$: Matrix Effect or Grain Size Effect?

What is the cause of the factor of 2 decrease in $\Gamma_{Mg/Al}$ in SiC compared to O-rich standards such as NIST glass and Burma spinel? Two plausible explanations are (i) SiC is O-free and thus chemically different from O-rich standards, i.e., different matrix chemistries, and $\Gamma_{Mg/Al}$ varies with matrix, and (ii) presolar SiC grains are smaller than polished NIST glass and Burma spinel, and $\Gamma_{Mg/Al}$ varies with grain size (Hoppe et al. 2023).

It is well known that the local O abundance increases the positive secondary ion yield of many elements in SIMS, such that "oxygen flooding" wherein a low pressure of O_2 is leaked into the analysis chamber is a common method for increasing SIMS yields (e.g., Zalm & Vriezema 1992). Since the electronegativities of Mg, Al, and Si all differ (e.g., Fan et al. 1992), one would expect that their relative yields should depend on the O abundance. Since O_2 flooding is not possible in the NanoSIMS, significant differences in yields for O-free phases like SiC compared to oxides or silicate glasses would be expected, strongly supporting possibility (i). Nevertheless, it is worth examining possibility (ii) in some detail.

In this study, we investigated possibility (ii) by analyzing Burma spinel grains of varying sizes (0.5–2 μm) for their Al–Mg isotopes with NanoSIMS, and an example of the results is shown in Figure A5 for illustration. Figure A5 reveals that the Al/Mg ratio determined by NanoSIMS analyses is significantly affected by an edge effect, i.e., increased Al/Mg ratios at grain rims, which is absent in the $^{26}Mg/^{24}Mg$ ratio image. Because of this edge effect, the measured $^{27}Al/^{24}Mg$ ratio increases from 2.0 to 2.6 for the largest (2.2 μm) and smallest (0.6 μm) grains in Figure A5, respectively, corresponding to a 30% decrease in $\Gamma_{Mg/Al}$ with decreasing grain size. It is, however, difficult to quantity the edge effect since it depends on the edge topography that varies on a case-by-case basis. A practical approach to suppress the edge effect is to exclude grain edges from the chosen ROIs for data reduction, which can be done for grains $\geq$500 nm given the thickness of the edge (>200 nm) and the spatial resolution of the NanoSIMS analyses ($\sim$100 nm; Figure A5). Excluding grain edges for data reduction is also necessary to suppress the effects of Al contamination rims on

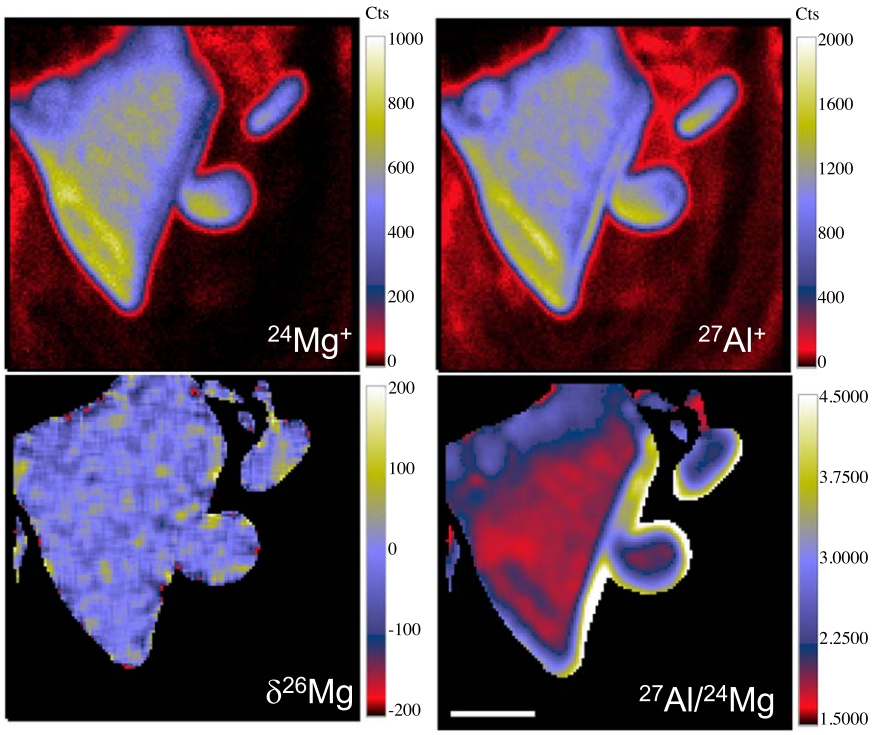

Figure A5. NanoSIMS Images of Burma spinel grains. The scale bar denotes 1 μm.

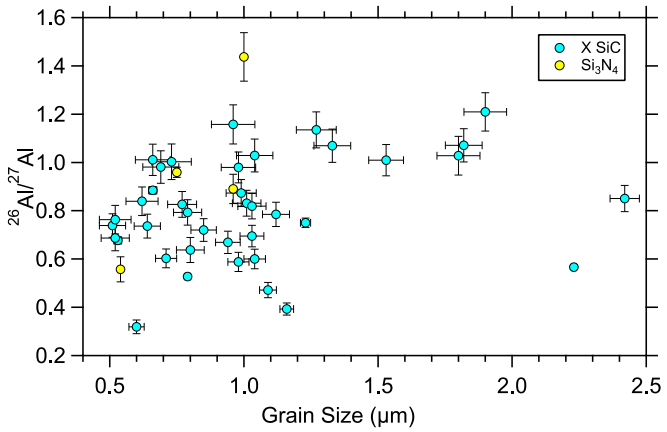

Figure A6. Initial $^{26}Al/^{27}Al$ ratios of X and Si_3N_4 grains from this study as a function of grain size.

the derived initial $^{26}Al/^{27}Al$ ratios for presolar SiC grains. Indeed, our derived $\Gamma_{Mg/Al}$ values based on polished NIST glass and large (>1 μm) Burma spinel grains are in good agreement within uncertainties (Section 2).

Based on the lack of dependence of the derived initial $^{26}Al/^{27}Al$ ratio on grain size among our X grains (Figure A6), we conclude that the factor of 2 decrease in $\Gamma_{Mg/Al}$ in SiC is most likely a result of the reduced chemistry of SiC in comparison to NIST 610 and Burma spinel. Given the lack of proper standards for Si_3N_4 grains, we also adopted $\Gamma_{Mg/Al} = 0.69$ for deriving the initial $^{26}Al/^{27}Al$ ratios of the four Si_3N_4 grains from this study.

Appendix B
Subtypes of Presolar X Grains

Figure A7 shows that the three subtypes of X grains from this study are indistinghuisable in their $^{12}C/^{13}C$, $^{14}N/^{15}N$, and inferred initial $^{26}Al/^{27}Al$ ratios.

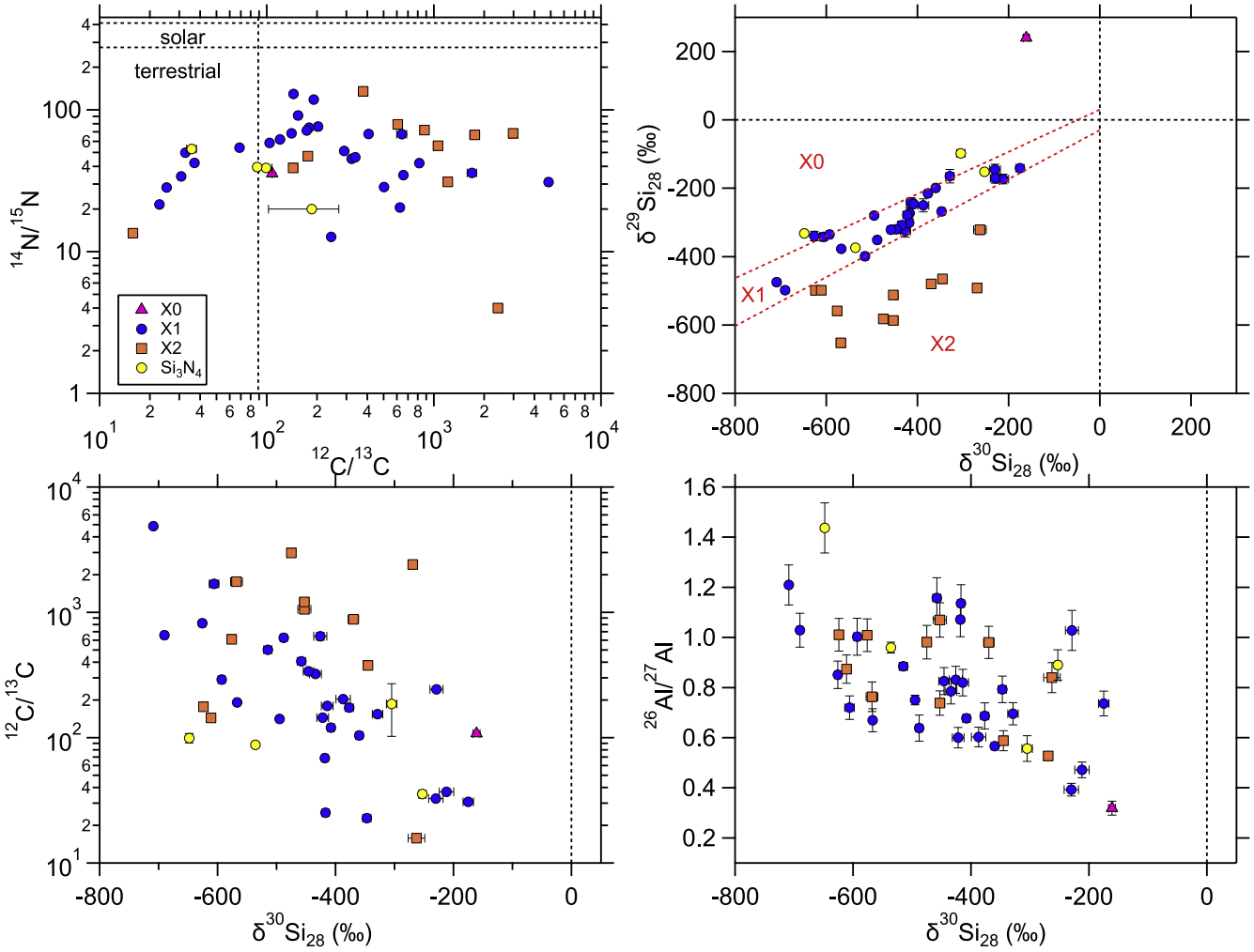

Figure A7. Plots comparing the isotopic compositions of the three subtypes of X grains that were initially proposed by Lin et al. (2010) and later modified by Stephan et al. (2021). Si_3N_4 grain data are also plotted for comparison.

Appendix C
Comparison of CCSN Grains with ν-models

X grains from this study are compared to ν-models in Figure A8. See Section 3.2 for detailed discussions on the data-model comparisions.

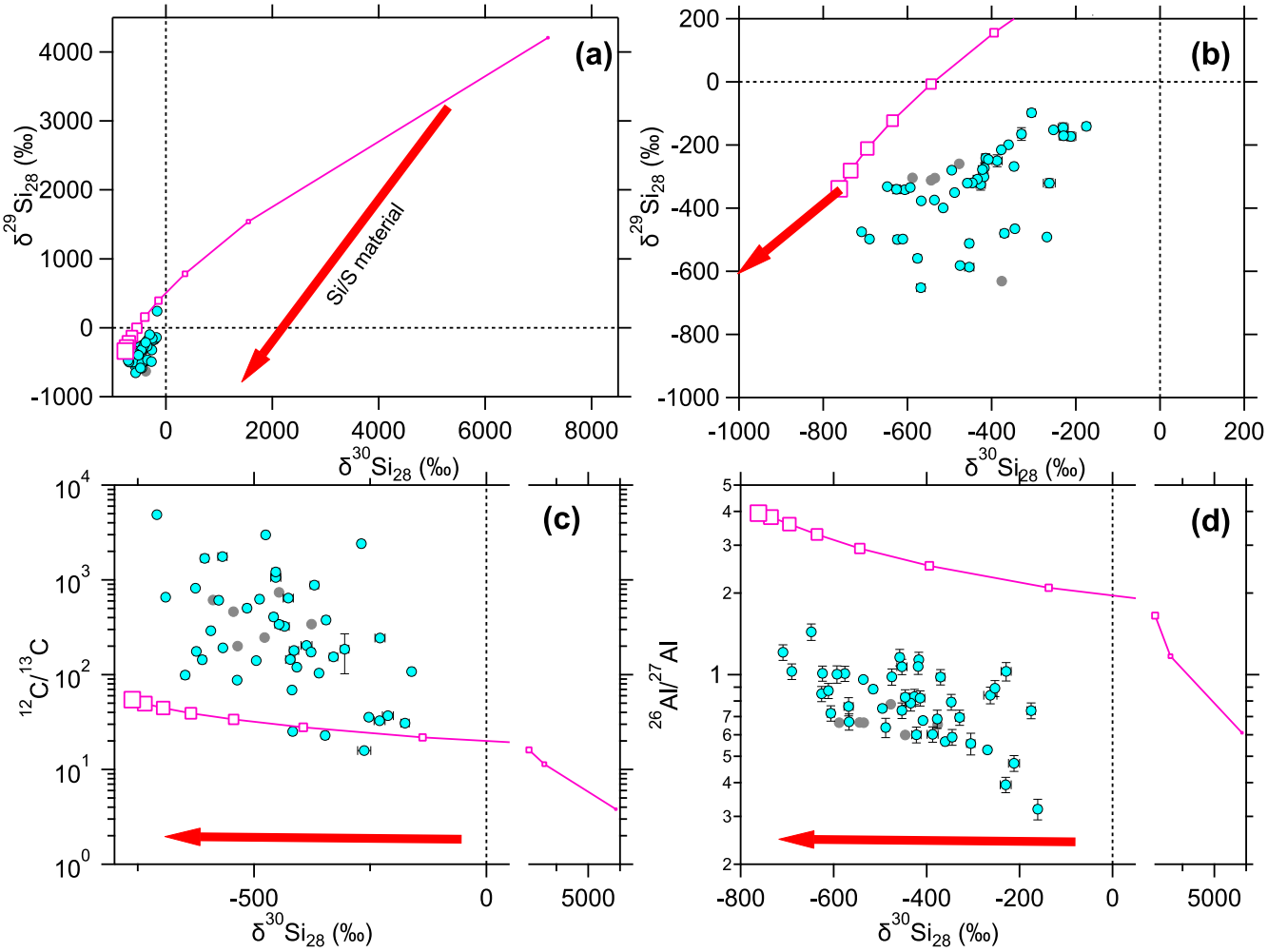

Figure A8. Same as Figure 3 except that the ν-model calculations for the Fe/Ni core are shown for comparisons .

ORCID iDs

Nan Liu https://orcid.org/0000-0002-4456-4065
Conel M. O'D. Alexander https://orcid.org/0000-0002-8558-1427
Bradley S. Meyer https://orcid.org/0000-0001-6307-9818
Larry R. Nittler https://orcid.org/0000-0002-5292-6089
Jianhua Wang https://orcid.org/0000-0002-7671-2413
Rhonda M. Stroud https://orcid.org/0000-0001-5242-8015

References

Bojazi, M. J., & Meyer, B. S. 2014, PhRvC, 89, 025807
Diehl, R. 2017, in IAU Symp. 331, Supernova 1987A: 30 years Later—Cosmic Rays and Nuclei from Supernovae and their Aftermaths, ed. A. Marcowith et al. (Cambridge: Cambridge Univ. Press), 157
Drouin, D., Couture, A. R., Joly, D., et al. 2007, Scanning, 29, 92
Fan, C.-Z., Jiang, N., & Qian, W.-J. 1992, ApSS, 62, 131
Groopman, E., Zinner, E., Amari, S., et al. 2015, ApJ, 809, 31
Hammer, N. J., Janka, H.-Th, & Müller, E. 2010, ApJ, 714, 1371
Hoppe, P., Leitner, J., & Amari, S. 2023, ApJL, 943, L22
Hwang, U., & Laming, J. M. 2012, ApJ, 746, 130
José, J., Hernanz, M., Amari, S., Lodders, K., & Zinner, E. 2004, ApJ, 612, 414
Kobayashi, C., Karakas, A. I., & Lugaro, M. 2020, ApJ, 900, 179
Limongi, M., & Chieffi, A. 2003, ApJ, 592, 404
Lin, Y., Gyngard, F., & Zinner, E. 2010, ApJ, 709, 1157
Liu, N., Alexander, C. M. O'D., Nittler, L. R., & Wang, J. 2023, in 54th Lunar and Planetary Science Conf., 2806 (Houston, TX: Lunar and Planetary Institute), 2496
Liu, N., Cristallo, S., & Vescovi, D. 2022, Univ, 8, 362
Liu, N., Nittler, L. R., Alexander, C. M. O'D., & Wang, J. 2018a, SciA, 4, eaao1054
Liu, N., Steele, A., Nittler, L. R., et al. 2017, M&PS, 52, 2550
Liu, N., Stephan, T., Boehnke, P., et al. 2018b, ApJ, 855, 144
Lodders, K., & Fegley, B., Jr. 1995, Metic, 30, 661
Malherbe, J., Penen, F., Isaure, M.-P., et al. 2016, AnaCh, 88, 7130
Meyer, B. S., Krishnan, T. D., & Clayton, D. D. 1998a, ApJ, 498, 808
Meyer, B. S., McLaughlin, G. C., & Fuller, G. F. 1998b, PRC, 58, 3696
Meyer, B. S., Weaver, T. A., & Woosley, S. E. 1995, Metic, 30, 325
Müller, B. 2020, LRCA, 6, 3
Nie, N. X., Wang, D. A., & Torrano, Z. A. 2023, Sci, 379, 372
Nittler, L. R., & Alexander, C. M. O' D. 2003, GeCoA, 67, 4961
Nittler, L. R., & Ciesla, F. 2016, ARA&A, 54, 53
Nittler, L. R., Hoppe, P., Alexander, C. M. O'D., et al. 1995, ApJL, 453, L25
Pearce, N. J. G., Perkins, W. T., Westgate, J. A., et al. 1997, GGRes, 21, 115
Pignatari, M., Wiescher, M., Timmes, F. X., et al. 2013, ApJL, 767, L22
Pignatari, M., Zinner, E., Hoppe, P., et al. 2015, ApJL, 808, L43
Rauscher, T., Heger, A., Hoffman, R. D., & Woosley, S. E. 2002, ApJ, 576, 323
Sandoval, M. A., Hix, W. R., Messer, O. E. B., Lentz, E. J., & Harris, J. A. 2021, ApJ, 921, 113
Schofield, J., Pignatari, M., Stancliffe, R. J., & Hoppe, P. 2022, MNRAS, 517, 1803
Sieverding, A., Waldrop, P. G., Harris, J. A., Hix, W. R., & Lentz, E. J. 2023, ApJ, 950, 34

Stephan, T., Bose, M., Boujibar, A., et al. 2021, in 52nd Lunar and Planetary Science Conf. (Houston, TX: Lunar and Planetary Institute), 2358
Stephan, T., & Trappitsch, R. 2023, IJMS, 491, 117053
Stephan, T., Trappitsch, R., Davis, A. M., et al. 2018, GeCoA, 221, 109
Takigawa, A., Miki, J., Tachibana, S., et al. 2008, ApJ, 688, 1382
Wongwathanarat, A., Janka, H.-T., Müller, E., et al. 2017, ApJ, 842, 13
Xu, Y., Zinner, E., Gallino, R., et al. 2015, ApJ, 799, 156
Zalm, P. C., & Vriezema, C. J. 1992, NIMPB, 64, 626